

# Hyperspectral Smoke Segmentation via Mixture of Prototypes

Lujian Yao, Haitao Zhao\*, Xianghai Kong, Yuhan Xu

*Automation Department, School of Information Science and Engineering, East China University of Science and Technology, Meilong Rd, No.130, Shanghai, 200237, China*

---

## Abstract

Smoke segmentation is critical for wildfire management and industrial safety applications. Traditional visible-light-based methods face limitations due to insufficient spectral information, particularly struggling with cloud interference and semi-transparent smoke regions. To address these challenges, we introduce hyperspectral imaging for smoke segmentation and present the first hyperspectral smoke segmentation dataset (HSSDataset) with carefully annotated samples collected from over 18,000 frames across 20 real-world scenarios using a *Many-to-One annotations* protocol. However, different spectral bands exhibit varying discriminative capabilities across spatial regions, necessitating adaptive band weighting strategies. We decompose this into three technical challenges: spectral interaction contamination, limited spectral pattern modeling, and complex weighting router problems. We propose a mixture of prototypes (MoP) network with: (1) Band split for spectral isolation, (2) Prototype-based spectral representation for diverse patterns, and (3) Dual-level router for adaptive spatial-aware band weighting. We further construct a multispectral dataset (MSSDataset) with RGB-infrared images. Extensive experiments validate superior performance across both hyperspectral and multispectral modalities, establishing a new paradigm for spectral-based smoke segmentation.

*Keywords:* Hyperspectral Smoke Segmentation, Prototype Learning, Industrial Application.

---

---

\*Corresponding Author.

## 1. Introduction

Smoke segmentation plays a crucial role in both wildfire management and industrial safety applications through its ability to precisely localize smoke presence. In wildfire scenarios, smoke segmentation serves as an early warning indicator, enabling rapid identification of fire sources and facilitating timely emergency response [1]. In industrial settings, accurate smoke segmentation helps detect gas leaks and hazardous emissions early, preventing potential accidents and enabling swift containment measures [2]. The broad applicability and critical safety implications make smoke segmentation an important research area with significant real-world impact.

Traditional smoke segmentation approaches primarily focused on analyzing specific smoke characteristics, including color space [3], textural analysis, and color enhancement strategies [4]. Vision-based techniques such as morphological operations [5], and transmission estimation [6] are extensively employed. However, these traditional methods struggled with the variability of smoke and often required manual parameter tuning for different environmental conditions and scenarios. Deep learning-based smoke segmentation approaches have made significant progress through several key strategies. Multi-scale feature fusion [7, 8] integrates features from multiple levels to capture both local details and global context, while receptive field expansion [9, 10] enables better understanding of smoke’s spatial extent and morphological variations. Progressive segmentation [11, 12] employs coarse-to-fine refinement to iteratively improve boundary delineation, and uncertainty quantification [13] helps handle ambiguous regions where smoke boundaries are unclear.

However, visible-light-based methods face critical limitations due to the narrow spectral range of visible light bands, which provides insufficient spectral information to distinguish smoke from visually similar phenomena. Similar to camouflaged object detection [14], where objects blend seamlessly with their surroundings, smoke segmentation also faces the challenge of detecting semi-transparent and low-contrast regions that blend with the background. Performance is easily constrained by two key challenges: **(1) Cloud interference:** Clouds and smoke exhibit similar visual characteristics, making it difficult to distinguish them in visible light images. **(2) Semi-transparent smoke regions:** Semi-transparency commonly appears along smoke edges with spatially varying opacity, low contrast against the background. These properties produce diffuse boundaries, leading to unclear transitions and in-

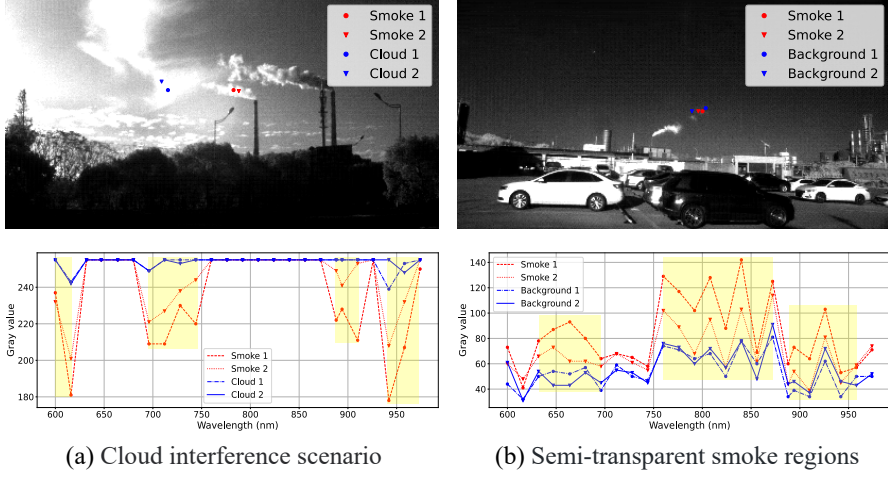


Figure 1: Motivation for hyperspectral smoke segmentation. The upper part shows challenging smoke scenarios with cloud interference and semi-transparent regions in the visible light band. The lower part plots the spectral distribution of the marked points. Yellow shaded regions highlight the key discriminatory band ranges where smoke and clouds (or smoke and background) exhibit the most significant spectral divergence.

consistent visual patterns that confuse segmentation models.

To address the limitations of visible light data, we introduce hyperspectral imaging for smoke segmentation. Hyperspectral imaging captures spectral information across several narrow, contiguous spectral bands, typically spanning the visible, near-infrared, and shortwave infrared regions of the electromagnetic spectrum. Each pixel in a hyperspectral image contains a spectral signature, forming a unique "spectral fingerprint" that characterizes the material composition and physical properties of the corresponding ground object. This spectral information is particularly valuable for smoke segmentation, as smoke particles exhibit distinct absorption and scattering properties across different wavelengths due to their size distribution, chemical composition, and temperature characteristics. The fine spectral resolution enables detection of subtle spectral variations that are invisible to conventional visible-light cameras, making it possible to differentiate between smoke and spectrally similar phenomena.

For example, in Figure 1(a), smoke and clouds appear nearly indistinguishable in visible light due to their similar white appearance. However, examining different hyperspectral bands reveals clear distinctions between

smoke and clouds in certain spectral ranges. In Figure 1(b), semi-transparent smoke regions that are difficult to differentiate from the background in visible light exhibit distinct spectral signatures across hyperspectral bands, enabling more reliable segmentation. These examples highlight how hyperspectral imaging provides critical discriminative information that is unavailable in conventional visible light images.

To promote this research area, we introduce the first hyperspectral smoke segmentation dataset (HSSDataset), built from an extensive collection of over 18,000 hyperspectral video frames captured across 20 real-world smoke scenarios using a hyperspectral camera with 25 spectral bands (600-974nm). From this large-scale raw data collection, we carefully selected and annotated 1,007 high-quality samples under diverse challenging conditions, including high exposure, low visibility, early-stage minimal smoke, cloud interference, and complex backgrounds. To ensure annotation reliability and capture the inherent uncertainty in smoke boundary delineation, we introduce a rigorous *Many-to-One annotations* protocol, where each frame receives three independent annotations from different annotators, and the final ground truth is determined through majority voting consensus.

However, directly applying hyperspectral data to smoke segmentation faces a fundamental challenge: **Different spectral bands have varying discriminative capabilities in different spatial regions.** For instance, some bands excel at capturing smoke transparency while others are more effective at distinguishing smoke from visually similar objects like clouds or fog. This regional-spectral variation necessitates adaptive *band weighting* strategies that can dynamically assign different spectral band weighting to different spatial regions. This variation creates three main technical challenges:

**❶ Spectral interaction contamination:** Simply employing convolution or transformer-based backbones can mix spectral channels, causing spectral interactions that contaminate the spectral signatures. Mixing bands with different discriminative purposes dilutes their respective capabilities, making it difficult to leverage band-specific characteristics. This issue is well-recognized in band selection literature [15, 16], where not all spectral bands contribute equally and redundant or noisy bands can degrade performance. Our ablation study (Table 6 and Figure 11) further validates the effectiveness of spectral isolation. **❷ Limited spectral pattern modeling capability:** Conventional approaches rely on monolithic feature encoders that cannot adequately capture the complex and diverse spectral patterns present in hyperspectral data. The diversity of spectral patterns requires specialized representation

learning for spectral patterns characterized by multiple distribution centers, where different spectral bands may exhibit distinct clustering patterns in the feature space, reflecting the diverse material compositions and physical properties of smoke across different wavelength ranges. **③ Weighting router problem:** Given the presence of spectral interaction contamination and the diversity of spectral patterns, determining optimal band weighting becomes highly complex. The weighting mechanism must adapt to varying input conditions and dynamically adjust weighting across different spatial regions to capture the intricate dependencies between spectral characteristics and spatial context.

To address these challenges, we propose a mixture of prototypes (MoP) network that leverages *prototype learning* to adaptively model diverse spectral patterns across hyperspectral bands. The core principle of MoP is to enable dynamic band weighting that automatically adapts to input-specific feature characteristics, allowing the model to emphasize the most discriminative spectral bands. Prototype learning is a representation learning approach where multiple prototype vectors serve as representative templates that capture different data patterns or categories.

Specifically, the MoP addresses these challenges through three key innovations: **(For ①) Band split** processes each spectral band independently through dedicated neural network branches, ensuring complete spectral isolation to preserve spectral signatures and eliminate interaction contamination. **(For ②) Prototype-based spectral representation** employs multiple specialized prototypes to capture diverse spectral patterns, with each prototype learning to encode specific spectral characteristics rather than using uniform representations. **(For ③) Dual-level router** addresses the weighting router problem with a two-stage mechanism that dynamically adjusts band weighting across spatial regions under varying input conditions. It first aggregates prototypes via the prototype router to capture intricate dependencies between spectral characteristics, then employs the feature router to produce spatial-aware band weighting.

To demonstrate the generalizability of our MoP, we further extend our validation beyond hyperspectral data by constructing a multispectral smoke segmentation dataset (MSSDataset) that contains RGB–infrared paired images. This MSSDataset comprises carefully annotated smoke samples across diverse scenarios. Our MoP achieves consistent superior performance on both hyperspectral and multispectral data.

Our main contributions can be summarized as follows:

- We introduce the first hyperspectral smoke segmentation task and establish a comprehensive hyperspectral smoke segmentation dataset (HSSDataset), employing a rigorous *Many-to-One annotations* protocol to ensure reliable ground truth.
- A novel mixture of prototypes (MoP) network is proposed that performs spatial-aware band weighting on input-specific features across diverse smoke scenarios.
- We develop three key innovations within the MoP: Band split for spectral isolation to preserve spectral signatures, prototype-based spectral representation for diverse pattern modeling, and dual-level router for adaptive weight allocation.
- To validate the generalizability of our MoP, we construct a complementary multispectral smoke segmentation dataset (MSSDataset) and demonstrate consistent superior performance across both hyperspectral and multispectral modalities.

## 2. Related Work

### 2.1. Smoke Segmentation

Traditional smoke segmentation approaches primarily focused on analyzing specific smoke characteristics, including color space transformations [3], textural analysis, and color enhancement strategies [4]. Vision-based techniques such as morphological operations [5], and transmission estimation [6] are extensively employed. While computationally efficient and easy to implement, these traditional methods struggled with the inherent variability of smoke and often required manual parameter tuning for different environmental conditions and scenarios.

Deep learning-based smoke segmentation approaches address the aforementioned challenges through several key strategies: (1) Multi-scale feature fusion: Methods such as [7, 8] integrate features from multiple abstraction levels to capture both local details and global context, essential for handling the multi-scale nature of smoke. (2) Receptive field expansion: Techniques including [9, 10] augment the perceptual field of neural networks to better capture the spatial extent of smoke and its morphological variations. By expanding the receptive field, these methods can better understand the global context and long-range dependencies that are crucial for accurate smoke

detection. (3) Coarse-to-fine refinement: Progressive segmentation strategies [11, 12] employ hierarchical processing to refine segmentation boundaries iteratively. These methods typically start with coarse predictions and progressively refine the results to achieve more precise boundary delineation. (4) Uncertainty quantification: Advanced methods [13] incorporate uncertainty estimation mechanisms to handle ambiguous regions and improve robustness in challenging scenarios where smoke boundaries are inherently unclear.

However, visible-light-based smoke segmentation methods face critical limitations due to the narrow spectral range of visible light bands, which provides insufficient discriminative information for complex scenarios.

### 2.2. Hyperspectral Image

Hyperspectral imaging captures data across hundreds of narrow, contiguous spectral bands [17, 18], forming a 3D data cube  $(h, w, d)$  where each pixel contains a rich spectral signature that characterizes material composition and physical properties [19, 20, 21]. This rich spectral information makes hyperspectral imaging particularly suitable for challenging smoke segmentation tasks, where conventional visible-light-based data struggles with cloud interference, varying transparency, and complex backgrounds.

Recent advances in hyperspectral image processing have explored diverse strategies for spectral-spatial feature extraction and fusion [22]. Our MoP differs from these generic approaches in two key aspects: (1) Existing methods such as spatial-spectral cross-fusion networks [23] and asymptotic spectral mapping [24] typically treat all spectral bands uniformly or apply fixed band selection, whereas our MoP enables *dynamic* and *spatial-aware* band weighting through band-level prototypes that adapts to input-specific features. (2) Methods like multi-source spectral data combination [25] and heterospectral structure compensation [26] rely on monolithic encoders for spectral processing, while our band split strategy ensures complete spectral isolation before adaptive weighting.

### 2.3. Prototype Learning and Mixture of Experts

Prototype learning originated from classical machine learning methods like nearest neighbor algorithms [27] and cognitive science theories on prototype representation [28]. At its core, prototype learning uses representative examples to model different classes, enabling classification by comparing samples to these prototypes. This approach led to various non-parametric classification methods such as learning vector quantization (LVQ) [29] and

neighborhood component analysis (NCA) [30]. Modern deep learning has embraced prototype learning by incorporating it into supervised [31], unsupervised [32], and self-supervised [33] frameworks, providing structured embedding spaces through multi-centric modeling.

Mixture of Experts (MoE) [34] involves training multiple specialized networks (experts) alongside a gating mechanism that determines which experts to activate for each input, allowing selective computation and specialized processing. Core MoE approaches include GShard [35] for transformer-based architectures and Switch Transformer [36] for sparse expert routing.

In our work, we integrate prototype learning with MoE to present a natural and promising direction for hyperspectral smoke segmentation. Prototype learning provides interpretable spectral representations, while MoE enables efficient processing of diverse spectral patterns through specialized Router networks. This combination allows our approach to maintain multiple specialized prototypes for different smoke characteristics while routing spectral features to the most appropriate expert.

### 3. Hyperspectral Smoke Segmentation Dataset (HSSDataset)

This section provides an overview of our dataset construction process, beginning with the hyperspectral camera system specifications and data collection methodology (Sec. 3.1). We then detail our annotation protocol and quality control measures (Sec. 3.2). Finally, we present the multispectral dataset extension for MoP validation (Sec. 3.3). Both the HSSDataset and MSSDataset are publicly available on Hugging Face<sup>1</sup>.

#### 3.1. Hyperspectral Camera System and Data Collection

Hyperspectral cameras combine imaging and spectroscopic technologies to simultaneously capture two-dimensional spatial and one-dimensional spectral information. We employ a XIMEA MQ022HG-IM-SM5X5-NIR hyperspectral camera with detailed specifications shown in Figure 2. This camera utilizes a specialized 25-band mosaic filter coating with a  $5 \times 5$  filter array deployed on the sensor surface. Each  $5 \times 5$  pixel block simultaneously acquires spectral information across 25 distinct bands, with wavelengths spanning 600-974nm: 600, 616, 632, 647, 664, 680, 696, 712, 728, 744, 760, 776, 792, 808, 824, 840, 856, 872, 888, 894, 910, 926, 942, 958, and 974 nm.

---

<sup>1</sup>Dataset: <https://huggingface.co/datasets/LujianYao/HSSDataset>

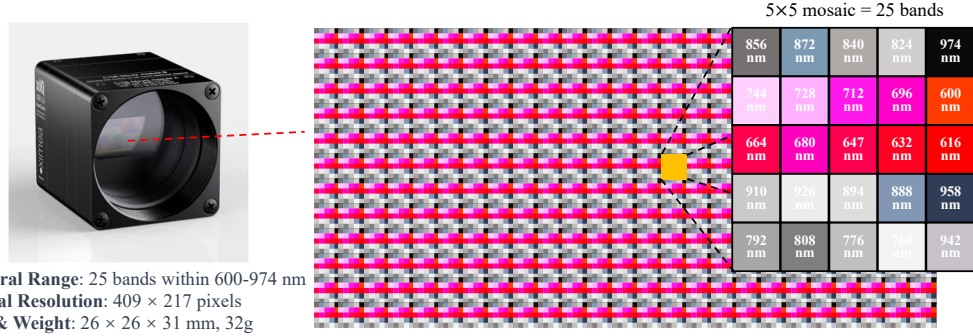


Figure 2: XIMEA MQ022HG-IM-SM5X5-NIR hyperspectral camera specifications and 25-band mosaic filter design. The camera employs a specialized  $5 \times 5$  filter array with wavelengths spanning 600-974nm for simultaneous spatial and spectral information.

The frame-style hyperspectral acquisition device based on mosaic coating, as illustrated in Figure 2, represents an advanced hyperspectral imaging technology developed using high-sensitivity CCD and sCMOS chips. This technology achieves hyperspectral imaging by coating different spectral band filters on individual detector pixels. The key advantages of this hyperspectral imaging approach include the ability to simultaneously balance spectral and spatial resolution, rapidly acquire both spectral and spatial information, and achieve high integration density.

As shown in Figure 3, we conduct data collection across 20 real-world industrial emission scenarios, capturing over 18,000 hyperspectral video frames. The collection targeted diverse smoke conditions, including challenging scenarios such as high exposure environments, low visibility conditions, and early-stage minimal smoke detection. We also addressed environmental interference from cloud and complex background elements, and varying atmospheric conditions. The dataset encompasses various smoke characteristics, including semi-transparent regions, blurred boundaries, and varying opacity and particle density across different industrial contexts. Table 1 provides a comprehensive breakdown of our 1,007 annotated samples across different challenging scenarios. The distribution covers both scene-based classifications and smoke-based classifications.

### 3.2. Dataset Annotation Protocol

**Sampling Strategy.** From the 18,000+ collected frames, we systematically sample every 18th frame to capture smoke evolution dynamics while main-

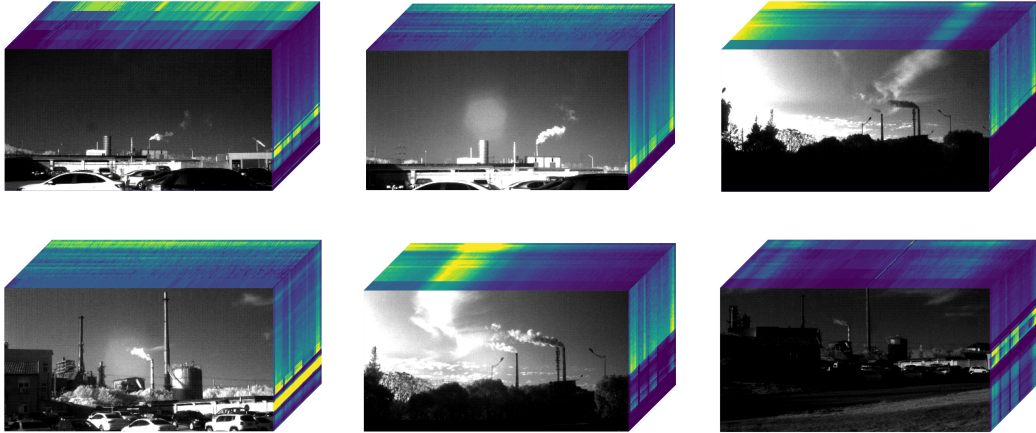


Figure 3: The challenging scenarios of HSSDataset.

Table 1: Distribution of annotated samples across different challenging scenarios in HSSDataset.

Scenario Category	Sample Count	Description
<b>Scene-based Classification</b>		
High Exposure	214	Bright lighting conditions with overexposed regions
Low Visibility	118	Poor lighting and atmospheric conditions
Complex Background	411	Industrial environments with cluttered backgrounds
Cloud Interference	264	Scenes with cloud-smoke confusion scenarios
<b>Smoke-based Classification</b>		
Early-stage Smoke	268	Small smoke plumes in initial emission phases
High Transparency Smoke	258	Varying smoke opacity and transparency
Complex-shaped Smoke	481	Irregular smoke patterns with unclear boundaries

taining annotation efficiency. This strategy ensures comprehensive coverage of smoke generation, diffusion, and dissipation phases.

**Band-Averaged Image Generation.** For annotation purposes, we generate band-averaged grayscale images by computing the arithmetic mean across all spectral bands of the hyperspectral data. This approach creates intuitive visual representations that facilitate human interpretation while preserving the overall spatial structure and intensity patterns of the smoke regions.

**Many-to-One Annotations.** To ensure annotation quality and handle the inherent ambiguity in smoke boundary delineation, we recruit nine trained expert annotators and implement a protocol where each selected frame receives three independent ground truth masks from three different annotators. All annotations are performed on the band-averaged grayscale images gener-

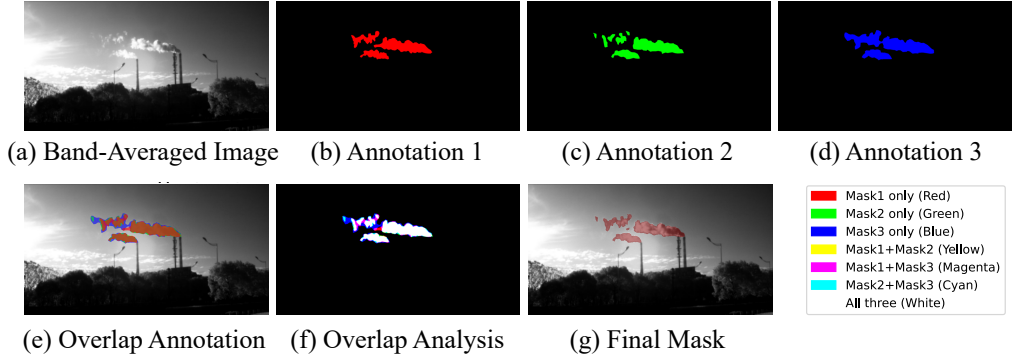


Figure 4: Many-to-One annotations for hyperspectral smoke segmentation.

ated from the hyperspectral data. This multi-annotator approach generates three separate segmentation masks per image, with special emphasis placed on challenging regions including early-stage minimal smoke, semi-transparent regions, and blurred boundaries. Figure 4 illustrates our Many-to-One Annotations process. The first row shows (a) the band-averaged grayscale image generated by averaging all spectral bands and (b-d) the three independent annotations from different annotators. As observed, different annotators exhibit varying judgments in transparent regions and smoke boundary areas, highlighting the inherent ambiguity in smoke segmentation. The overlapped annotation visualization (e) displays all masks superimposed together, while the overlap analysis (f) uses different colors to represent regions with varying consensus levels, clearly revealing that annotators have significant disagreements in transparent areas and edge regions. The final mask (g) represents our ground truth, where each pixel is classified as smoke if at least two annotators identify it as smoke, otherwise it is classified as background.

**Ground Truth Definition.** Final ground truth masks are generated through *majority voting*, where each pixel is classified as smoke if at least two-thirds of annotators label it as smoke. The resulting binary masks assign value 1 to smoke regions and value 0 to background areas. This approach effectively handles annotation uncertainty while preserving reliable boundaries, ultimately producing 1,007 high-quality annotated hyperspectral samples.

**Inter-Annotator Agreement Statistics.** Among all pixels marked as smoke by at least one annotator, unanimous agreement (3/3) accounts for 52.07%, majority agreement (2/3) for 14.14%, and single annotator only (1/3) for 33.79%. In terms of the final ground truth (pixels with  $\geq 2/3$  agree-

ment), 78.63% come from unanimous agreement and 21.37% from majority agreement, confirming that our Many-to-One majority voting approach effectively filters uncertain annotations.

### 3.3. Multispectral Smoke Segmentation Dataset (MSSDataset)

To further validate the effectiveness of our proposed method, we construct an additional multispectral dataset (MSSDataset) with raw data from FLAME2 [37]. Figure 5 shows representative RGB-IR frame pairs with enhanced IR visualization. We carefully annotate 200 samples across diverse scenarios. Each sample contains distinct smoke features suitable for annotation. The final MSSDataset provides multispectral cubes encompassing RGB plus infrared channels. This configuration allows us to evaluate our method’s performance on different spectral data compositions beyond the 25-band hyperspectral setting. The dataset captures diverse scenarios, including wildland fire smoke under various environmental conditions.

## 4. Methodology

In this section, we first present the overall idea of MoP (Sec. 4.1) and then detail its three key components: band split (Sec. 4.2), prototype-based spectral representation (Sec. 4.3), and dual-level router (Sec. 4.4). Finally, we describe the decoder head and loss function (Sec. 4.5). For easy reference, the definitions of symbols are provided in Tab 3.

### 4.1. Overview of Mixture of Prototypes (MoP)

The core of MoP is to enable dynamic band weighting that automatically adapts to input-specific feature characteristics, allowing the model to emphasize the most discriminative spectral bands for each individual smoke scenario while suppressing less informative spectral information.

As illustrated in Figure 6, given a hyperspectral image, our MoP pipeline operates through the following stages: First, the input is processed by two

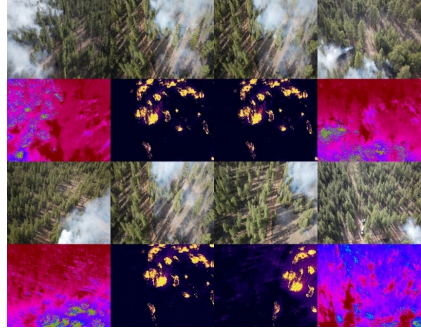


Figure 5: Visible and infrared frame pairs in MSSDataset.

Table 2: Hyperparameter configuration.

Parameter	Value	Description
<i>Training Configuration</i>		
Learning Rate	6e-5	Initial learning rate for AdamW optimizer
Batch Size	4	Batch size for training
Weight Decay	0.01	L2 regularization weight
Training Iterations	40,000	Total training iterations
LR Schedule	Polynomial	Learning rate annealing policy
Optimizer	AdamW	Optimization algorithm
<i>Data Augmentation</i>		
Input Size	512 × 512	Image resolution for HSSDataset
Input Size	512 × 512	Image resolution for MSSDataset
Random Scaling	0.5-2.0	Random scaling range
Random Crop	Enabled	Random cropping augmentation
Random Flip	Enabled	Horizontal flipping augmentation
<i>MoP-Specific Parameters</i>		
$\lambda$	0.01	Weight for pixel-prototype contrastive loss
$K$	3	Number of prototypes per class per band
$D$	250	Feature dimension
$\tau$	0.1	Temperature for contrastive learning
$\mu$	0.999	Momentum coefficient for prototype update
$\varepsilon$	0.05	Entropy regularization in Sinkhorn
Sinkhorn Iterations	3	Iterations for Sinkhorn-Knopp algorithm
Groups ( $G$ )	25	Number of groups for band split (HSS)
Groups ( $G$ )	4	Number of groups for band split (MSS)

Table 3: Symbol notation.

Symbol	Description
<i>Basic Variables</i>	
$\mathbf{I} \in \mathbb{R}^{h \times w \times d}$	Hyperspectral input image
$\mathbf{X}_{\text{com}}, \mathbf{X}_{\text{indi}}$	Common and individual branch features
$\mathbf{X}_{\text{MoP}}$	MoP-enhanced features
$h, w, d$	Height, width, spectral bands
$H, W, D$	Feature height, width, dimension
$N$	Number of spatial locations
<i>Prototype Learning</i>	
$\mathbf{p}_{c,k}^{(b)} \in \mathbb{R}^{D/d}$	Prototype $k$ for class $c$ and band $b$
$\mathbf{P}_c^{(b)} \in \mathbb{R}^{(D/d) \times K}$	Prototype matrix for class $c$ and band $b$
$\mathbf{X}_c^{(b)} \in \mathbb{R}^{N \times (D/d)}$	Feature matrix for class $c$ and band $b$
$\mathbf{M}_c^{(b)} \in \mathbb{R}^{K \times N}$	Assignment matrix for class $c$ and band $b$
$K, C$	Number of prototypes per band, number of classes
$c, b, k$	Class index, band index, prototype index
<i>Dual-level Router</i>	
$\alpha_{c,k}^{(b)}$	Prototype aggregation weights
$\mathbf{p}_{\text{agg},c}^{(b)}$	Aggregated prototype for class $c$ and band $b$
$\beta \in \mathbb{R}^d$	Band-level importance weights
$\mathbf{p}_{\text{concat}}$	Concatenated prototypes
<i>Loss Functions</i>	
$\mathcal{L}_{\text{CE}}, \mathcal{L}_p$	Cross-entropy and pixel-prototype losses
$\lambda, \tau, \mu$	Loss weight, temperature, momentum
$\varepsilon$	Entropy regularization parameter
$y_i, \hat{y}_i$	Ground truth and predicted labels

parallel branches: (1) individual branch: an individual encoder  $\mathbf{f}_I$  that applies band split to extract features from each spectral band independently, preserving spectral signatures ( $\mathbf{X}_{\text{indi}}$ ); and (2) a common branch: an common encoder  $\mathbf{f}_C$  that follows conventional segmentation approaches, processing all spectral bands jointly to provide general spatial-semantic understanding ( $\mathbf{X}_{\text{com}}$ ). Next, features from the individual branch undergo band weighting through our dual-level router, which takes  $\mathbf{X}_{\text{indi}}$  and band-level prototypes as inputs to generate weighted features  $\mathbf{X}_{\text{MoP}}$ . The prototypes are dynamically updated through momentum-based learning during training while remaining fixed during inference. Finally, the weighted features  $\mathbf{X}_{\text{MoP}}$  are fused with features  $\mathbf{X}_{\text{com}}$  from the common branch and passed through a decoder head (a  $1 \times 1$  convolution that maps from  $D$  dimensions to 2 classes) to produce the final segmentation results.

#### 4.2. Band Split.

**Intuition.** Traditional band selection methods [15] operate directly on raw spectral channels without feature expansion or enhancement, which severely limits their effectiveness in deep network pipelines. Conventional deep learning backbones, including convolution and transformer, inherently perform computations across the channel dimension when processing hyperspectral data. These cross-channel operations inevitably lead to mixing and interaction between different spectral bands, causing spectral contamination that

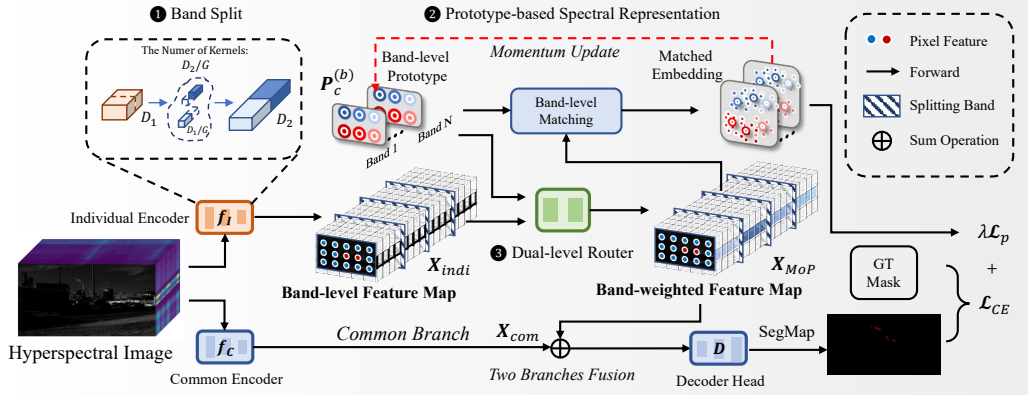


Figure 6: Overall architecture of our mixture of prototypes (MoP) network.

compromises the independent characteristics of each band and dilutes the spectral signatures. To address these limitations, we propose a band-level split strategy that processes each spectral band independently.

### Implementation.

**Individual Branch Design.** The individual branch is built upon the MiT [38] architecture with key modifications to achieve band split through *group convolution* with the number of groups equal to the band count ( $G = 25$ ). This design naturally ensures spectral isolation, as each group processes one band independently, while maintaining parameter efficiency and computational scalability through the grouped architecture (see Figure 7). For a hyperspectral input  $\mathbf{I} \in \mathbb{R}^{h \times w \times d}$  with  $d = 25$  bands, the individual branch applies grouped convolutions with  $G = 25$  groups to extract band-specific features  $\mathbf{X}_{\text{indi}} \in \mathbb{R}^{H \times W \times D}$ , while the common branch processes the full input to generate  $\mathbf{X}_{\text{com}} \in \mathbb{R}^{H \times W \times D}$ , where  $D = 250$  is the feature dimension.

**Feature Representation.** For convenience in subsequent computations, we uniformly adopt the flattened representation, which transforms 2D spatial feature maps into 1D sequences to facilitate pixel-prototype matching via the Sinkhorn algorithm. Each spectral band is represented by exactly 10 channels ( $D/d = 10$ ). For each band  $b$ , we denote the band-specific features by  $\mathbf{X}_{\text{indi}}^{(b)} \in \mathbb{R}^{N \times (D/d)}$ , where  $N = H \times W$  is the number of spatial locations after flattening.

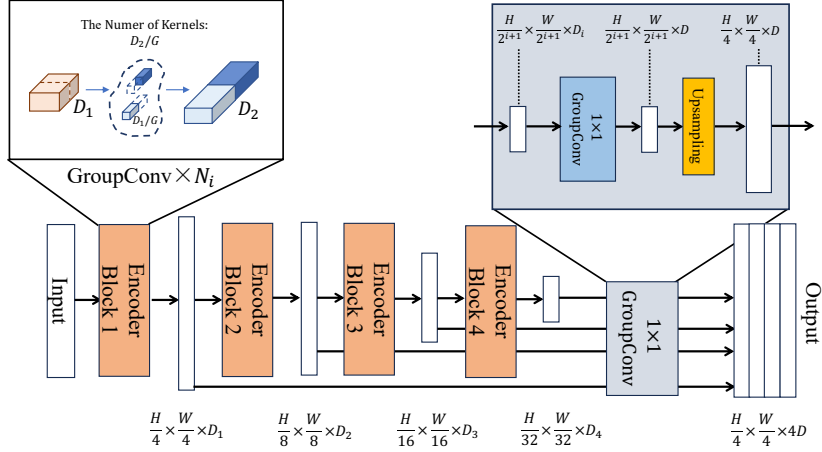


Figure 7: The individual branch is built upon the MiT architecture with key modifications to achieve band split through group convolution with the number of groups equal to the band count ( $G = 25$ ).

#### 4.3. Prototype-based Spectral Representation (Band-level Prototype).

**Intuition.** Common approaches rely on monolithic feature encoders that cannot adequately capture the complex and diverse spectral patterns present in hyperspectral data. We propose prototype-based spectral representation, which offers advantages by learning *band-level prototypes*. Each prototype encodes the overall features of its corresponding spectral band. This enables the model to learn comprehensive spectral signatures that maintain consistency across different samples while preserving the discriminative ability.

#### Implementation.

**Prototype Definition.** For each class  $c$  (smoke/background), we define  $K$  prototypes  $\mathbf{p}_{c,k}^{(b)} \in \mathbb{R}^{D/d}$  for each spectral band  $b$ . The matrix expression of these prototypes is  $\mathbf{P}_c^{(b)} = \{\mathbf{p}_{c,k}^{(b)}\}_{k=1}^K \in \mathbb{R}^{(D/d) \times K}$ .

**Pixel-Prototype Matching.** For each spectral band, we perform pixel-level matching between spectral features and prototypes to establish correspondence and update prototype representations. The matching process employs the Sinkhorn-Knopp algorithm to solve the optimal transport problem [39]:

$$\mathbf{M}_c^{(b)} = \text{Sinkhorn} \left( \mathbf{P}_c^{(b)}, \mathbf{X}_c^{(b)}, \varepsilon \right), \quad (1)$$

where  $\mathbf{P}_c^{(b)} \in \mathbb{R}^{(D/d) \times K}$  represents the prototype matrix for class  $c$  and band

$b$ ,  $\mathbf{X}_c^{(b)} \in \mathbb{R}^{N \times (D/d)}$  denotes the spectral feature matrix for class  $c$  and band  $b$ , and  $\mathbf{M}_c^{(b)} \in \mathbb{R}^{M \times N}$  is the assignment matrix for class  $c$  and band  $b$ . It should be noted that  $\mathbf{X}_c^{(b)}$  is obtained by using ground truth labels (*during training only*) to get the class-specific features from the individual-branch features  $\mathbf{X}_{\text{indi}}^{(b)}$ . During inference, the prototypes remain fixed and are used directly in the dual-level router without requiring class-specific feature extraction. For notational simplicity, we omit the 'indi' marker and write  $\mathbf{X}_c^{(b)}$ . The assignment matrix  $\mathbf{M}_c^{(b)} \in \mathbb{R}^{M \times N}$  computes assignment probabilities. The detailed implementation of the Sinkhorn algorithm can be found in Algorithm 2. A common approach to implement prototype learning effectiveness is through prototype contrastive learning loss, which enforces discriminative prototype representations by maximizing similarity between pixels and their assigned prototypes while minimizing similarity with negative prototypes. The detailed formulation is presented in Sec. 4.5.

**Prototype Learning and Update.** The prototypes are initialized using truncated normal initialization with standard deviation 0.02. The prototypes are dynamically updated during training through a momentum-based learning mechanism. Each prototype is updated as:

$$\mathbf{p}_{c,k}^{(b)} \leftarrow \mu \mathbf{p}_{c,k}^{(b)} + (1 - \mu) \bar{\mathbf{i}}_{c,k}^{(b)}, \quad (2)$$

where  $\mu = 0.999$  is the momentum coefficient, and  $\bar{\mathbf{i}}_{c,k}^{(b)}$  indicates the  $\ell_2$ -normalized, mean vector of the embedded training pixels, which are assigned to prototype  $\mathbf{p}_{c,k}^{(b)}$  by pixel-prototype matching.

#### 4.4. Dual-level Router.

**Intuition.** The dual-level router addresses the adaptive weighting router problem by decomposing it into prototype aggregation and band weighting two sequential stages. Our design enables spatial-aware weighting allocation based on input-specific features, allowing the model to adaptively emphasize the most discriminative spectral bands for different smoke scenarios.

#### Implementation.

**Dual-Level Router Architecture.** As illustrated in Figure 8, the dual-level router consists of two sequential stages: Proto-Router and Feature-Router, each addressing distinct optimization challenges. Our dual-level router processes individual branch features  $\mathbf{X}_{\text{indi}}$  through a two-stage routing mechanism that adaptively weights both prototypes and spectral bands. To clearly illustrate the dual-level routing process, we describe the operations for a single pixel feature  $\mathbf{x}_{\text{indi}} \in \mathbb{R}^D$ .

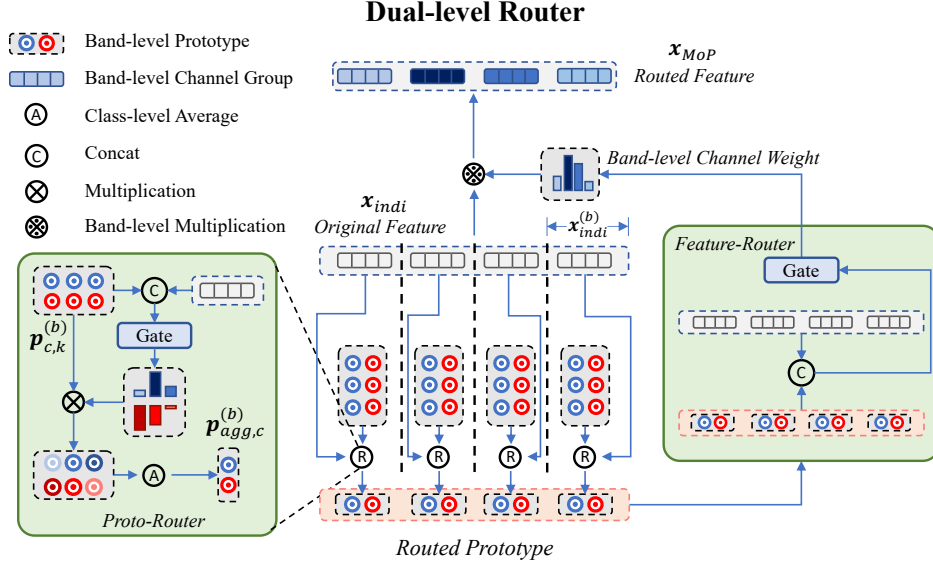


Figure 8: The pipeline of dual-level router. *Note: For visual clarity, this schematic illustrates the routing process using four spectral bands as a simplified example; the actual system operates on all 25 spectral bands.*

**Stage 1: Prototype Router.** The prototype router operates at the band level to adaptively aggregate multiple prototypes into a single representative prototype for each class when  $K > 1$  prototypes exist per band. For each spectral band  $b$ , it processes band-specific features and corresponding prototype candidates:

$$\alpha_{c,k}^{(b)} = \text{ProtoRouter}(\mathbf{x}_{\text{indi}}^{(b)}, \{\mathbf{p}_{c,k}^{(b)}\}_{c,k}), \quad (3)$$

where  $\mathbf{x}_{\text{indi}}^{(b)} \in \mathbb{R}^{(D/d)}$  represents the band-specific feature vector for a single pixel with channel dimension  $D/d$ ,  $\{\mathbf{p}_{c,k}^{(b)}\}_{c,k}$  are the prototype candidates for band  $b$  with matching channel dimension 10, and  $\alpha_{c,k}^{(b)}$  are the prototype aggregation weights. The aggregated prototypes for each band are computed:

$$\mathbf{p}_{\text{agg},c}^{(b)} = \sum_{k=1}^K \alpha_{c,k}^{(b)} \cdot \mathbf{p}_{c,k}^{(b)}, \quad (4)$$

**Stage 2: Feature Router.** The feature router operates on the complete feature representation to generate adaptive band-level weighting. For a single

pixel, it takes the full individual feature vector and concatenated band-level prototypes as input:

$$\boldsymbol{\beta} = \text{FeatureRouter}(\mathbf{x}_{\text{indi}}, \mathbf{p}_{\text{concat}}), \quad (5)$$

where  $\mathbf{x}_{\text{indi}} \in \mathbb{R}^D$  represents the complete individual branch feature vector for a single pixel,  $\mathbf{p}_{\text{concat}} \in \mathbb{R}^{C \times D}$  concatenates all band-level aggregated prototypes  $\mathbf{p}_{\text{agg},c}^{(b)}$  for  $C$  classes (resulting in  $C \times D$  channels), and the channel-level concatenation  $[\mathbf{x}_{\text{indi}}, \mathbf{p}_{\text{concat}}] \in \mathbb{R}^{(1+C) \times D}$  creates a  $3 \times D$ -dimensional input for  $C = 2$  classes. The output  $\boldsymbol{\beta} \in \mathbb{R}^D$  provides band-level importance weighting that is expanded via repetition to match the full feature dimension for element-wise multiplication with  $\mathbf{x}_{\text{indi}}$ .

**Final Output.** The dual-level router produces adaptively weighted individual features through band-level importance weighting:

$$\mathbf{x}_{\text{MoP}} = \text{Repeat}(\boldsymbol{\beta}, D/d) \odot \mathbf{x}_{\text{indi}}, \quad (6)$$

where  $\text{Repeat}(\boldsymbol{\beta}, (D/d)) \in \mathbb{R}^D$  expands the 25-dimensional band-level weights to match the full feature dimension by replicating each band weight across its  $(D/d)$  corresponding channels, and  $\mathbf{x}_{\text{MoP}} \in \mathbb{R}^D$  represents the adaptively weighted individual branch feature vector for a single pixel feature. Note that the above description uses a single pixel feature as an example for clarity. In practice, we extend this operation to the entire image level, with detailed implementation provided in Algorithm 1.

#### 4.5. Decoder Head and Loss Function

**Dual-Branch Feature Fusion.** Our decoder head processes features from two parallel branches to generate the final segmentation predictions. The architecture integrates both common spectral features  $\mathbf{X}_{\text{com}}$  and MoP-enhanced individual band  $\mathbf{X}_{\text{MoP}}$  features through a fusion mechanism. The two branches are combined through element-wise averaging to leverage both common context and adaptive spectral weighting:

$$\mathbf{X}_{\text{fusion}} = \frac{\mathbf{X}_{\text{com}} + \mathbf{X}_{\text{MoP}}}{2} \quad (7)$$

The fused features  $\mathbf{X}_{\text{fusion}}$  are processed through a simple but effective decoder head consisting of a convolutional layer followed by softmax activation to generate the final segmentation predictions.

**Loss Function.** Our training objective consists of two complementary components: a standard segmentation loss and a pixel-prototype contrastive loss.

**Pixel-Prototype Contrastive Learning.** The regular way of prototype learning lies in learning discriminative feature space through contrastive learning between features and prototypes [40]. The intuition is to enforce each pixel feature vector  $\mathbf{x}_{indi_i}^{(b)}$  to be similar to its assigned ('positive') prototype  $\mathbf{p}_{c_x, k_x}^{(b)}$  and dissimilar to other irrelevant 'negative' prototypes  $\mathcal{P}^{-(b)}$ :

$$\mathcal{L}_p = -\log \frac{\exp(\mathbf{x}_{indi_i}^{(b)\top} \mathbf{p}_{c_x, k_x}^{(b)} / \tau)}{\exp(\mathbf{x}_{indi_i}^{(b)\top} \mathbf{p}_{c_x, k_x}^{(b)} / \tau) + \sum_{\mathbf{p}^- \in \mathcal{P}^{-(b)}} \exp(\mathbf{x}_{indi_i}^{(b)\top} \mathbf{p}^- / \tau)}, \quad (8)$$

where the temperature  $\tau = 0.1$  controls the concentration level of representations.

**Segmentation Loss.** For the final segmentation task, we employ the standard binary cross-entropy loss:

$$\mathcal{L}_{CE} = -\frac{1}{N} \sum_{i=1}^N [y_i \log(\hat{y}_i) + (1 - y_i) \log(1 - \hat{y}_i)], \quad (9)$$

where  $\hat{y}_i$  represents the predicted probability for pixel  $i$ , and  $y_i$  is the ground truth label.

**Total Loss.** The complete training objective combines both components:

$$\mathcal{L}_{total} = \mathcal{L}_{CE} + \lambda \mathcal{L}_p, \quad (10)$$

where  $N$  is the total number of pixels,  $y_i \in \{0, 1\}$  is the ground truth binary label for pixel  $i$  (1 for smoke, 0 for background),  $p_i$  is the predicted probability of pixel  $i$  being smoke, and  $\lambda$  is set to 0.01 following the configuration established in prior prototype learning literature [40].

## 5. Experiments

This section provides experiments and analysis. Section 5.1 presents the datasets, baselines, implementation, and backbone configurations. Section 5.2 reports overall benchmark results on HSSDataset and MSSDataset, including comparisons under real-time vs accuracy-oriented settings, scale-aware analysis, and qualitative visualizations. Section 5.3 conducts module-wise ablations of band split, band-level prototype, and dual-level router. Section 5.4 further studies design choices and hyperparameters.

### 5.1. Experimental Setup

**Datasets.** Our experiments are conducted on two datasets: (1) HSSDataset: Our newly constructed hyperspectral smoke segmentation dataset containing 1,007 samples across 25 spectral bands (600-974nm). The dataset covers diverse challenging scenarios, including high exposure, low visibility, early-stage minimal smoke, cloud interference, and complex backgrounds. The annotated samples are split into training, validation, and test sets with a ratio of approximately 6:2:2. (2) MSSDataset: A multispectral dataset with RGB-IR paired samples derived from the FLAME2 dataset [37], providing 4-channel spectral information. Due to the scale of this dataset, the annotated samples are split into training, validation, and test sets with a ratio of approximately 8:1:1 to ensure sufficient training data. To comprehensively evaluate performance, we further conduct scale-aware evaluation by categorizing smoke into small, medium, and large scales, with the partition criteria following FoSp [41].

**Baseline Comparisons.** As this is the first work for hyperspectral smoke segmentation, we evaluate against various strong segmentation baselines, including CNN-based approaches (PSPNet [42], DeepLabV3+ [43], OCR-Net [44], SegNeXt [45], Trans-BVM [13]), Transformer-based methods (SegFormer [38], Mask2Former [46], ProtoSeg [40], FoSp [41]), where Trans-BVM and FoSp are specifically designed for smoke segmentation. We reproduce these methods and adapt them to hyperspectral data by only modifying the input channels from 3 to 25 while keeping other components unchanged.

**Implementation Details.** We implement our method using PyTorch on the MMSegmentation. All experiments are conducted on NVIDIA RTX 3090Ti GPUs. For data augmentation during training, we adopt standard techniques including random horizontal flipping, random scaling (0.5-2.0), and random cropping. The input hyperspectral images are resized to  $512 \times 512$  for training, while maintaining the original aspect ratio during inference. We utilize the AdamW optimizer with an initial learning rate of 6e-5, weight decay of 0.01, and momentum parameters  $\beta_1 = 0.9$  and  $\beta_2 = 0.999$ . The learning rate is scheduled using polynomial annealing with a power of 0.9. Training is conducted for 40,000 iterations with a batch size of 4. For the MoP, we set the number of prototypes  $K = 3$  and the feature dimension  $D = 250$ . Hyperparameters setting are detailed in Table 2.

**Backbone configuration.** As shown in Table 4, to ensure fair comparison, we organize methods into two categories: real-time and accuracy-oriented settings, with backbone-specific comparisons within each category. For the real-

Table 4: Quantitive comparison on hyperspectral smoke segmentation benchmarks. We compare methods from various domains, including CNN-based and Transformer-based approaches across real-time and accuracy-oriented settings. The best: **bold**, the second: underline.

	Methods	Backbone Category	Small		Medium		Large		Total		Params	Flops
			$F_1$	$mIoU$	$F_1$	$mIoU$	$F_1$	$mIoU$	$F_1$	$mIoU$		
Real-Time	PSPNet [42]	CNN-based	49.32	35.87	64.14	47.80	71.39	55.93	61.23	46.07	13.6	53.0
	DeepLabv3+ [43]		53.50	39.68	63.79	47.59	<u>73.12</u>	<u>58.10</u>	62.92	47.82	15.2	68.6
	OCRNet [44]		43.83	32.17	61.23	46.62	69.47	54.52	59.26	46.20	12.1	53.6
	SegNeXt [45]		48.24	33.17	64.74	48.38	70.57	54.86	60.80	45.06	4.3	6.4
	SegFormer [38]	Transformer-based	53.48	37.78	65.63	49.21	70.17	54.33	62.87	46.84	3.8	6.9
	FoSp [41]		<u>56.90</u>	<u>40.40</u>	65.77	49.48	72.69	55.65	64.99	48.97	5.8	23.1
	ProtoSeg [40]		55.86	39.56	<u>67.83</u>	<u>51.72</u>	72.49	55.37	<u>65.43</u>	<u>49.53</u>	4.5	18.8
	MoP (ours)		<b>59.41</b>	<b>46.32</b>	<b>71.19</b>	<b>56.27</b>	<b>74.17</b>	<b>59.33</b>	<b>68.13</b>	<b>53.84</b>	4.4	7.3
Accuracy-Oriented	PSPNet [42]	CNN-based	59.09	43.35	70.95	55.64	77.40	63.53	68.80	53.73	49.0	178.9
	DeepLabv3+ [43]		57.78	41.56	<u>72.04</u>	<u>56.91</u>	77.50	<u>64.91</u>	69.11	54.03	43.6	176.6
	Trans-BVM [13]		58.76	43.51	71.81	56.79	76.41	64.66	69.44	54.80	47.3	185.2
	OCRNet [44]		48.27	37.58	68.27	53.34	77.51	64.15	64.20	51.08	70.4	162.6
	SegNeXt [45]		62.54	47.04	68.59	53.43	73.92	59.37	68.72	53.57	48.9	65.7
	Mask2Former [46]	Transformer-based	57.31	41.47	69.41	53.63	76.44	62.16	67.34	51.94	99.4	208.2
	SegFormer [38]		64.99	48.95	67.80	51.68	75.34	60.75	68.90	53.21	30.6	44.7
	FoSp [41]		<u>67.34</u>	<u>51.72</u>	70.60	55.01	77.48	63.50	<u>71.38</u>	<u>56.21</u>	47.5	49.2
	ProtoSeg [40]		66.00	51.27	68.96	53.18	<u>77.54</u>	63.48	71.15	56.11	45.4	42.4
	MoP (ours)		<b>69.32</b>	<b>54.56</b>	<b>73.89</b>	<b>59.03</b>	<b>78.50</b>	<b>65.15</b>	<b>73.63</b>	<b>59.21</b>	11.4	11.5

time setting, we adopt a customized MiT-B0 [38]: we modify (i) the patch-embedding to accept 25-channel hyperspectral input and (ii) the `num_layers` = [2, 2, 2, 2], while using stage-wise channels `in_channels` = [25, 50, 125, 200]. For the accuracy-oriented setting, we use a customized MiT-B3 with the same `in_channels` and `num_layers` = [3, 4, 16, 3]. Other architectural components remain unchanged. The individual branch uses  $N_i$  identical to `num_layers` for both settings.

**Evaluation Metrics.** Following previous literature [13, 41], we employ  $F_1$  score and  $mIoU$  as our primary evaluation metrics.

## 5.2. Benchmark Results

**Hyperspectral Smoke Segmentation Dataset.** As shown in Table 4, in the *real-time* setting, our MoP achieves better performance across all scales. For small smoke scenarios, MoP achieves 59.41%  $F_1$  score and 46.32%  $mIoU$ , significantly outperforming the previous best Transformer-based method FoSp by 2.51% and 5.92%, respectively. For the total test set, our MoP achieves the best results with 68.13%  $F_1$  and 53.84%  $mIoU$  overall while maintaining computational efficiency (4.4M parameters, 7.3G FLOPs). For *accuracy-oriented* settings, our method demonstrates superior performance across all scenarios. MoP achieves 73.63%  $F_1$  score and 59.21%  $mIoU$ , outperforming

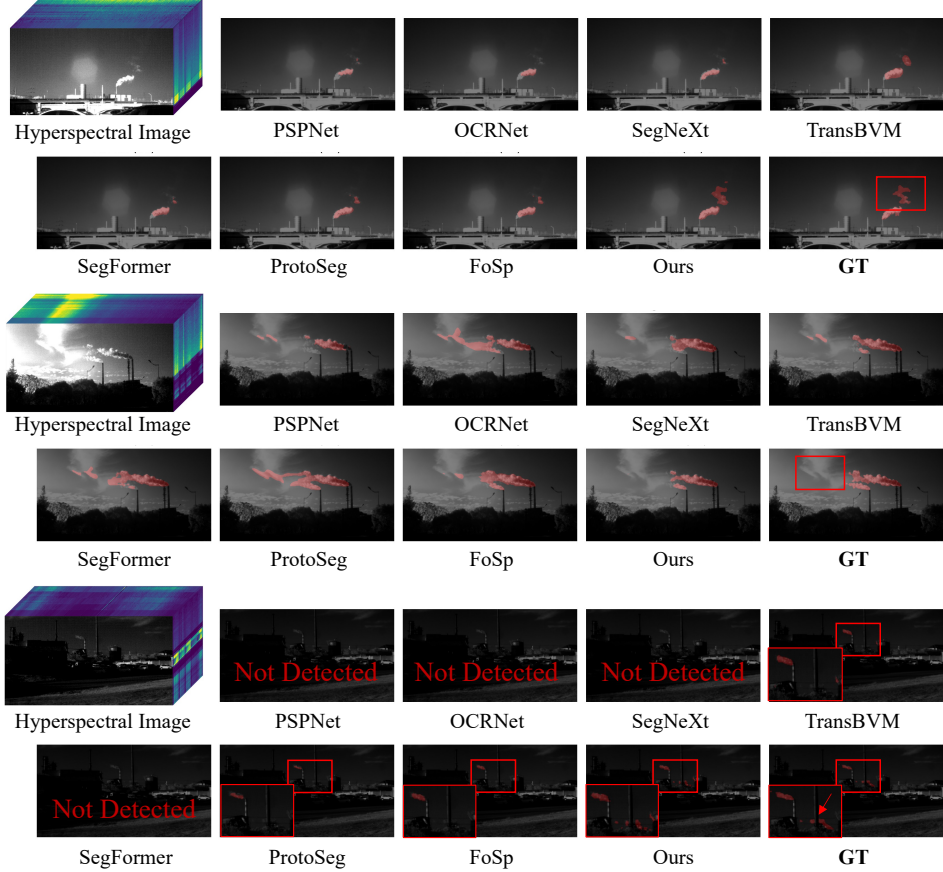


Figure 9: Visualization of HSSDataset segmentation results. For better visualization, the segmentation masks are overlaid on the band-averaged images.

the previous best method FoSp by 2.25% and 3.00% respectively. Particularly noteworthy is the significant improvement in small smoke (69.32%  $F_1$ ), which is crucial for early fire detection applications.

**Multispectral Smoke Segmentation Dataset.** Table 5 demonstrates the effectiveness of our method on the MSSDataset, which consists of RGB-IR paired multispectral data. Since the smoke scale in MSS is generally larger, we report results on the medium and large subsets. In the real-time setting, our MoP achieves 83.90%  $F_1$  score and 74.45% mIoU. For accuracy-oriented settings, our method achieves strong performance with 88.11%  $F_1$  and 79.55% mIoU, demonstrating effectiveness on multispectral data.

**Qualitative Analysis.** Figure 9 presents visual comparisons of our hyper-

Table 5: Quantitive comparison on MSSDataset. We compare methods from various domains, including CNN-based and Transformer-based approaches across real-time and accuracy-oriented settings. The best: **bold**, the second: underline.

	Methods	Backbone Category	Medium		Large		Total		Params	Flops
			$F_1$	$mIoU$	$F_1$	$mIoU$	$F_1$	$mIoU$		
Real-Time	PSPNet [42]	CNN-based	83.56	<u>74.44</u>	92.02	85.82	80.67	71.92	4.3	6.2
	Deeplabv3+ [43]		80.15	67.42	89.89	81.77	81.87	70.06	3.7	6.4
	OCRNet [44]		84.09	73.96	87.97	79.23	<u>82.80</u>	72.12	12.1	52.8
	SegNeXt [45]		80.11	67.27	90.15	82.16	81.34	69.63	5.8	22.9
	SegFormer [38]	Transformer-based	83.37	74.05	<u>92.06</u>	<u>86.36</u>	82.67	<u>72.87</u>	13.6	52.6
	FoSp [41]		84.27	74.08	90.38	82.80	82.43	71.71	15.2	68.4
	ProtoSeg [40]		81.29	68.90	91.05	83.65	82.27	70.96	4.4	18.2
	MoP (ours)		<b>85.50</b>	<b>75.70</b>	<b>93.24</b>	<b>87.70</b>	<b>83.90</b>	<b>74.45</b>	5.7	5.1
Accuracy-Oriented	PSPNet [42]	CNN-based	83.66	73.92	<u>93.11</u>	87.26	85.51	76.91	49.0	178.5
	Deeplabv3+ [43]		83.90	73.94	92.43	86.09	83.72	73.85	70.4	161.8
	SegNeXt [45]		84.46	73.44	92.29	85.78	86.26	76.36	45.3	41.4
	OCRNet [44]		83.40	71.96	91.13	83.80	85.40	75.06	48.9	65.3
	Trans-BVM [13]		84.01	73.30	91.78	84.88	86.19	76.26	43.4	176.2
	Mask2Former [46]	Transformer-based	81.04	68.72	90.33	82.52	84.47	73.74	44.6	29.5
	SegFormer [38]		84.70	73.83	91.52	84.44	86.04	76.00	99.2	207.8
	FoSp [41]		<u>84.88</u>	<u>74.14</u>	91.45	84.34	<u>86.61</u>	<u>76.81</u>	47.3	185.2
	ProtoSeg [40]		82.34	70.52	90.78	83.25	85.48	75.14	47.5	49.2
	MoP (ours)		<b>85.16</b>	<b>75.12</b>	<b>93.41</b>	<b>87.74</b>	<b>88.11</b>	<b>79.55</b>	15.1	13.9

spectral smoke segmentation results on three challenging scenarios in the HSSDataset: transparent smoke, cloud interference, and small smoke in low-light conditions. For transparent smoke cases, our method preserves fine boundary details and captures subtle transparency variations compared to baselines that only detect main smoke regions. In cloud interference scenarios, while baselines often confuse smoke and clouds, our MoP effectively differentiates them using distinct spectral signatures. For small smoke in low-light conditions where several baselines fail completely, our method successfully detects minimal smoke. Figure 10 shows our method maintains consistent performance on the MSSDataset.

**About the Computational Overhead.** Our MoP achieves a *low parameter* mainly because we reduce redundant channels without sacrificing performance, and the individual branch relies heavily on group convolutions, which add very few parameters. When transferring to the MSSDataset, the model has slightly more parameters because fewer groups lead to more parameters: we set  $G = 25$  for HSS and  $G = 4$  for MSS.

### 5.3. Ablation Study

**Effect of Band Split.** As shown in Table 6 (a), band split improves performance (+1.69%  $F_1$ , +1.55% mIoU on HSS) by preserving spectral signatures. Figure 11 validates this through correlation analysis: Common features show

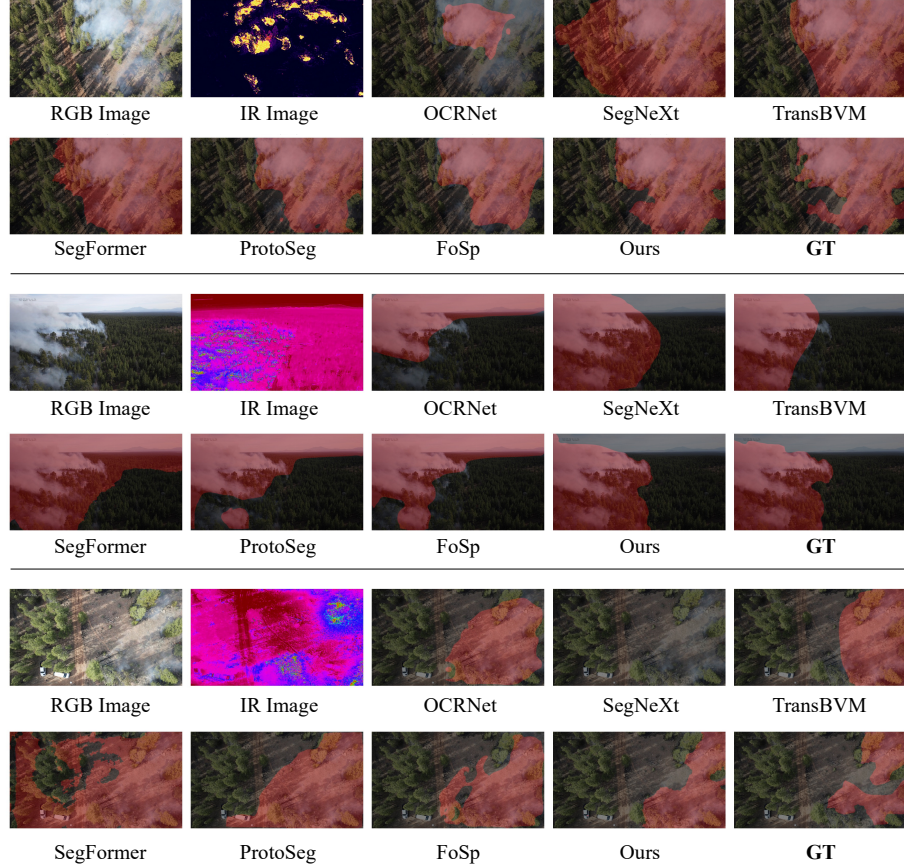


Figure 10: Visualization of MSSDataset segmentation results. For better visualization, the segmentation masks are overlaid on the RGB images.

high inter-channel correlations indicating spectral contamination, while band split features have low correlations demonstrating successful spectral isolation. The correlation distributions and per-channel analysis confirm that band split effectively maintains spectral purity.

**Effect of Band-level Prototype.** As reported in Table 6 (b), adding band-level prototype achieves cumulative improvements of 71.11%  $F_1$  and 56.10% mIoU on HSSDataset (+2.82%  $F_1$ , +2.94% mIoU over baseline), demonstrating the effectiveness of prototype-based spectral representation. Compared to band split alone, this adds +1.13%  $F_1$  and +1.39% mIoU. Figure 12 provides t-SNE visualization of the learned feature space, showing that our band-level proto component produces more clustered and discriminative feature

Table 6: Ablation study of our MoP components on HSS and MSS datasets. The “bl” (baseline) refers to the common branch only.

	Band Split	Band-level Proto	Feature Router	Proto Router	HSSDataset		MSSDataset	
					$F_1$	$mIoU$	$F_1$	$mIoU$
bl					68.29	53.16	84.23	73.15
(a)	✓				69.98 $\uparrow 1.69$	54.71 $\uparrow 1.55$	85.41 $\uparrow 1.18$	74.28 $\uparrow 1.13$
(b)	✓	✓			71.11 $\uparrow 2.82$	56.10 $\uparrow 2.94$	85.67 $\uparrow 1.44$	74.89 $\uparrow 1.74$
(c)	✓		✓		71.56 $\uparrow 3.27$	56.61 $\uparrow 3.45$	86.18 $\uparrow 1.95$	75.44 $\uparrow 2.29$
(d)	✓	✓	✓		72.91 $\uparrow 4.62$	58.46 $\uparrow 5.30$	87.42 $\uparrow 3.19$	78.41 $\uparrow 5.26$
(e)	✓	✓	✓	✓	<b>73.63 <math>\uparrow 5.34</math></b>	<b>59.21 <math>\uparrow 6.05</math></b>	<b>88.11 <math>\uparrow 3.88</math></b>	<b>79.55 <math>\uparrow 6.40</math></b>

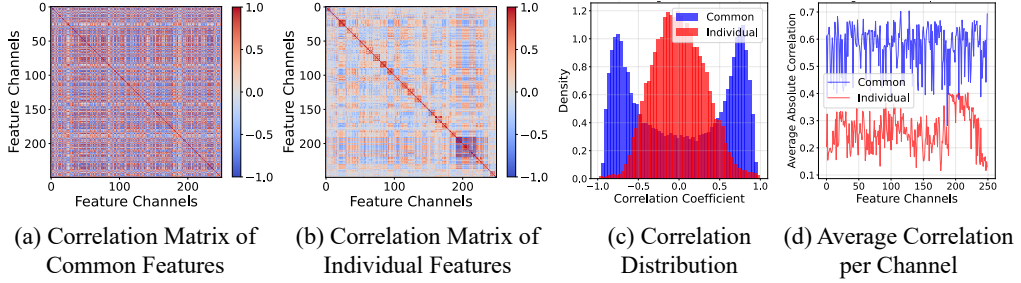


Figure 11: Qualitative analysis of the band split.

representations compared to baseline methods.

### Effect of Dual-Level Router.

We analyze the two components in order. *Feature Router*: Compared to band split (a→c), adding the feature router brings about +1.58%  $F_1$  and +1.90%  $mIoU$ , indicating that spatial-aware band weighting is an important component for leveraging varying band dis-

criminability. *Proto Router*: On top of band-level prototype + feature router (d→e), introducing the proto router yields an additional +0.72%  $F_1$  and +0.75%  $mIoU$ , confirming that prototype aggregation before band weighting provides complementary gains. As illustrated in Figure 13, we visualize the mean values of feature maps to compare the effects of dual-level router band weighting versus without band weighting. The visualization demon-

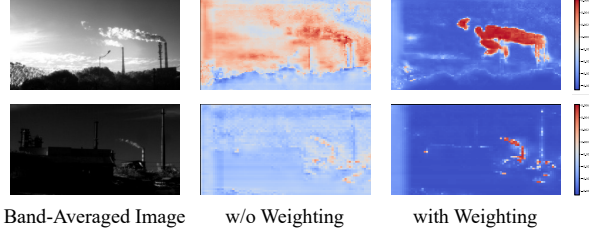


Figure 13: Effect of dual-level router visualized through feature map mean activations.

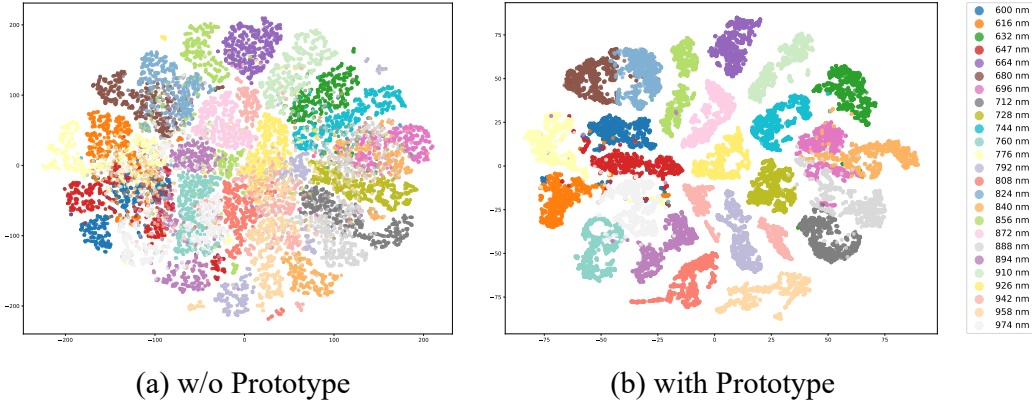


Figure 12: t-SNE visualization. The band-level prototype produces more clustered and discriminative features than baselines.

strates how the dual-level router enhances feature discrimination by adaptively weighting spectral bands. For interference scenarios (first row), the band weighting mechanism enables the model to produce higher mean activation values in smoke regions while effectively suppressing background interference from clouds and sky compared to the unweighted version. For small smoke in low-light conditions (second row), the weighted feature maps show significantly enhanced mean values in smoke regions, making them more distinguishable from the background compared to the unweighted counterpart.

**Component Contribution Analysis.** As evidenced in Table 6, band split and feature router demonstrate the most pronounced individual effects. Band split provides the fundamental foundation with  $+1.69\% F_1$  improvement, establishing the importance of independent spectral processing. Feature router shows the largest single-component contribution ( $+1.58\% F_1$  when added to band split), highlighting that adaptive spectral weighting is crucial for capturing the varying discriminability across different spectral bands.

**Weighting Distribution.** The visualization in Figure 14 demonstrates the distribution of weighting across different spectral bands. Through model learning, we observe that different wavelengths exhibit varying discriminative capabilities. For this particular scene, some bands are primarily effective for smoke, while others excel at background discrimination. Certain bands show relatively weak discriminative power, and some bands focus on different aspects of the scene. For instance, the 942nm band shows heightened attention to the smoke-emitting column, indicating its specialized sensitivity

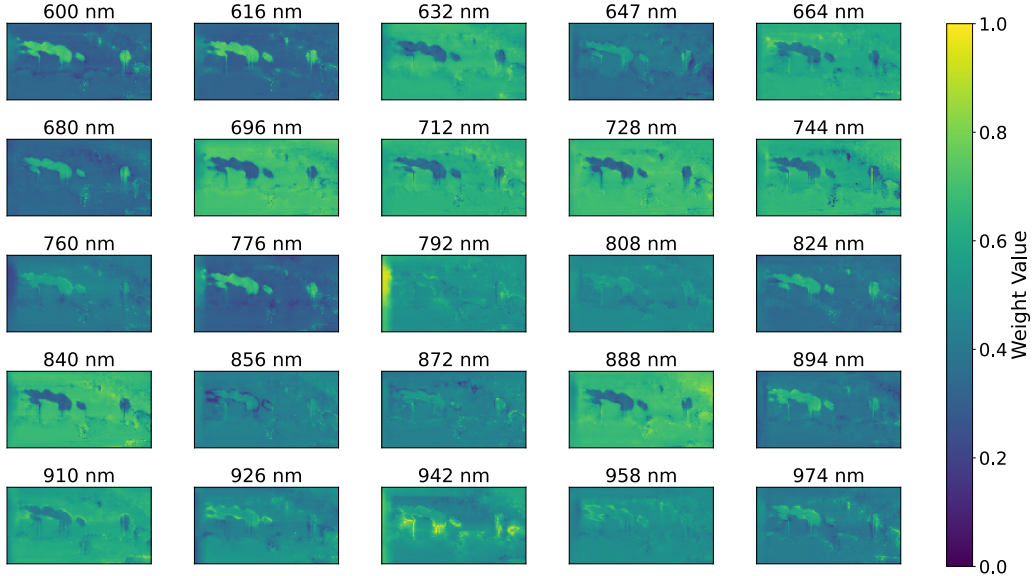


Figure 14: Visualization of adaptive spectral band weighting learned by dual-level router.

to specific scene elements.

#### 5.4. Other Ablation Studies

**The Number of Prototypes.** The number of prototypes  $K$  significantly impacts performance. With  $K = 3$ , our method achieves optimal performance (73.63% F1, 59.21% mIoU). Too few experts ( $K = 1$ ) limit the model’s ability to capture diverse spectral patterns, while too many experts ( $K = 4, 5$ ) introduce redundancy and potential overfitting.

**The Feature Dimension.** The feature dimension  $D$  determines the representational capacity of our prototype features. With  $D = 250$ , our method achieves the best performance. Lower dimensions ( $D = 50, 100$ ) lack sufficient representational power, while higher dimensions ( $D = 500$ ) may lead to overfitting and increased computational overhead.

Table 7: Analysis of key hyperparameters.

Parameter	Value	HSSDataset	
		$F_1$	$mIoU$
Prototype Number ( $K$ )	1	71.85	57.12
	2	72.94	58.31
	3	<b>73.63</b>	<b>59.21</b>
	4	73.21	58.87
	5	73.16	58.63
Feature Dimension ( $D$ )	50	71.92	57.68
	100	72.84	58.52
	150	73.15	58.76
	200	73.27	58.91
	250	<b>73.63</b>	<b>59.21</b>
	300	73.42	59.05
	500	73.18	58.87

Table 8: Ablation study of feature fusion strategies.

Fusion Strategy	HSS		MSS	
	$F_1$	$mIoU$	$F_1$	$mIoU$
Common Only	70.12	54.98	85.34	76.12
Individual Only	71.89	56.23	86.67	77.89
Concatenation	72.85	57.45	87.23	78.34
Element-wise Sum	<b>73.63</b>	<b>59.21</b>	<b>88.11</b>	<b>79.55</b>

Table 9: Ablation study of prototype update strategies.

Method	HSS		MSS	
	$F_1$	$mIoU$	$F_1$	$mIoU$
Gradient	72.73	58.08	87.78	78.41
Momentum	<b>73.63</b>	<b>59.21</b>	<b>88.11</b>	<b>79.55</b>

**Prototype Update Strategy.** We compare different prototype update strategies in Table 9. The gradient-based approach, while providing direct optimization through backpropagation, suffers from training instability and overfitting. In contrast, the momentum-based update achieves better performance by balancing stability and adaptability.

**Fusion Strategy.** Table 8 compares different ways to combine the common and individual branches. Individual only outperforms common only, demonstrating that individual only already achieves excellent performance and validates the effectiveness of our band split design. Element-wise sum achieves the best performance while requiring minimal computational overhead compared to concatenation (HSS: +0.56%  $F_1$ , +1.12%  $mIoU$ ), indicating that this lightweight fusion strategy not only reduces model complexity but also enhances feature integration.

## 6. Conclusion

**Conclusion.** In this work, we introduce the first hyperspectral smoke segmentation task to address the limitations of visible-light-based data in handling cloud interference and semi-transparent smoke regions. We establish the HSSDataset with high-quality annotations across diverse scenarios using a rigorous Many-to-One protocol. To tackle varying discriminative capabilities of spectral bands, we propose a mixture of prototypes (MoP) network with three key components: band split for spectral isolation, prototype-based representation for diverse patterns, and dual-level router for adaptive weighting. We further validate our approach on a multispectral dataset (MSS-Dataset), demonstrating superior performance across both hyperspectral and multispectral settings. We hope this introduced hyperspectral imaging opens new possibilities for developing more accurate and reliable smoke segmentation systems that can provide earlier warnings and reduce false alarms,

thereby improving emergency response and protecting lives and property.

**Limitation.** While our method provides an effective strategy for hyperspectral smoke segmentation, our approach employs relatively simple methods in certain components. Specifically, our band split strategy relies on basic group convolution for spectral isolation, and the dual-branch fusion mechanism uses straightforward element-wise averaging. Future work could explore more sophisticated band split techniques and advanced fusion strategies to achieve further performance improvements.

---

**Algorithm 1** Dual-Level Router (PyTorch-like).  $D$ : feature dimension,  $d$ : number of spectral bands,  $D/d$ : channels per band.

---

**Require:**  $X_{\text{indi}}: \mathbb{R}^{H \times W \times D}$ ,  $\text{proto\_indi}: \mathbb{R}^{C \times K \times d \times D/d}$   
**Ensure:**  $X_{\text{MoP}}: \mathbb{R}^{H \times W \times D}$

```

# Variable definitions: n: pixels, b=d: spectral bands, c: classes, ch=D/d: channels per band, k: prototypes per class
1: # Feature Preprocessing
2: N = H * W
3: _feat = X_indi.view(N, D)                                ▷ Flatten for processing
4: _feat_grouped = rearrange(_feat, 'n (b ch) -> n b ch', b=d) ▷ Group by bands
5: # Prototype Router
6: _proto_mul = rearrange(proto_indi, 'c k b ch -> 1 b (c k ch)')
7: _proto_mul = repeat(_proto_mul, '1 b ch -> n b ch', n=N)
8: concat_feature = torch.cat([_feat_grouped, _proto_mul], dim=-1)
9: _concat_flat = rearrange(concat_feature, 'n b ch -> (n b) ch')
10: weight_proto = F.softmax(self.gate_proto(_concat_flat), dim=-1)
11: weight_proto = rearrange(weight_proto, '(n b) ch -> n b ch', b=d)
12: weight_proto = repeat(weight_proto, 'n b ch 1 -> n b ch ch', ch=D/d)
13: _proto_weighted = weight_proto * _proto_mul
14: _proto_agg = _proto_weighted.mean(dim=3)                  ▷ Aggregate prototypes
15: _proto_indi = rearrange(_proto_agg, 'n b c ch -> n (b c ch)')
16: # Feature Router
17: concat_feature = torch.cat([_feat, _proto_indi], dim=-1)
18: weight = F.softmax(self.gate(concat_feature), dim=-1)    ▷ d band weights
19: weight = repeat(weight, 'n b -> n b ch', ch=D/d)       ▷ Expand to channels
20: weight = rearrange(weight, 'n b ch -> n (b ch)')
21: _weighted_feature = weight * _feat                      ▷ Element-wise multiplication
22: # Reshape to Image Dimensions
23: X_MoP = _weighted_feature.view(H, W, D)                ▷ Return features

```

---

---

**Algorithm 2** Sinkhorn Algorithm (PyTorch-like)

---

**Require:**  $P$ : band-level prototypes  $\mathbb{R}^{d \times K}$ ,  $X$ : band-level features  $\mathbb{R}^{d \times N}$ ,  $\text{iters}=3$ ,  $\text{epsilon}=0.05$

**Ensure:**  $M$ : pixel-to-prototype assignment  $\mathbb{R}^{K \times N}$

```
1:  $M = \text{torch.mm}(P.\text{transpose}(0, 1), X)$             $\triangleright$  Matrix multiplication:  $[K, N]$ 
2:  $M = \text{torch.exp}(M / \text{epsilon})$                     $\triangleright$  Apply exponential with temperature
3:  $M /= \text{torch.sum}(M)$                             $\triangleright$  Normalize to probability
4: for  $\text{iter}$  in  $\text{range}(\text{iters})$  do
5:   # Normalize each row
6:    $M /= \text{torch.sum}(M, \text{dim}=1, \text{keepdim=True})$        $\triangleright$  Row normalization
7:    $M /= K$                                                $\triangleright$  Scale by number of prototypes
8:   # Normalize each column
9:    $M /= \text{torch.sum}(M, \text{dim}=0, \text{keepdim=True})$        $\triangleright$  Column normalization
10:   $M /= N$                                               $\triangleright$  Scale by number of pixels
11: end for
12: # Make sure the sum of each column to be 1
13:  $M *= N$                                                $\triangleright$  Rescale final assignment matrix
14: return  $M$ 
```

---

## References

- [1] Evangelos Zervas, A. Mpimpoudis, Christos Anagnostopoulos, Odysseas Sekkas, and Stathes Hadjiefthymiades. Multisensor data fusion for fire detection. *Information Fusion*, 12(3):150–159, 2011.
- [2] Sapdo Utomo, Ayush Pratap, Periyasami Karthikeyan, John Ayeelyan, Hsiu-Chun Hsu, and Pao-Ann Hsiung. When explainable artificial intelligence meets data governance: Enhancing trustworthiness in multi-modal gas classification. *Information Fusion*, 125:103440, 2026.
- [3] Deng Xing, Yu Zhongming, Wang Lin, and Li Jinlan. Smoke image segmentation based on color model. *Journal on Innovation and Sustainability RISUS*, 6(2):130–138, 2015.
- [4] Yang Jia, Jie Yuan, Jinjun Wang, Jun Fang, Qixing Zhang, and Yongming Zhang. A saliency-based method for early smoke detection in video sequences. *Fire technology*, 52:1271–1292, 2016.
- [5] Alexander Filonenko, Danilo Cáceres Hernández, and Kang-Hyun Jo. Fast smoke detection for video surveillance using CUDA. *IEEE Transactions on Industrial Informatics*, 14(2):725–733, 2018.

- [6] Chengjiang Long, Jianhui Zhao, Shizhong Han, Lu Xiong, Zhiyong Yuan, Jing Huang, and Weiwei Gao. Transmission: a new feature for computer vision based smoke detection. In *Artificial Intelligence and Computational Intelligence*, pages 389–396. Springer, 2010.
- [7] Feiniu Yuan, Lin Zhang, Xue Xia, Qinghua Huang, and Xuelong Li. A gated recurrent network with dual classification assistance for smoke semantic segmentation. *IEEE Transactions on Image Processing*, 30:4409–4422, 2021.
- [8] Feiniu Yuan, Zeshu Dong, Lin Zhang, Xue Xia, and Jinting Shi. Cubic-cross convolutional attention and count prior embedding for smoke segmentation. *Pattern Recognition*, 131:108902, 2022.
- [9] Tao Jing, Qing-Hao Meng, and Hui-Rang Hou. SmokeSeger: A Transformer-CNN coupled model for urban scene smoke segmentation. *IEEE Transactions on Industrial Informatics*, 20(2):1385–1396, 2024.
- [10] Xiuqing Li, Zhenxue Chen, Q. M. Jonathan Wu, and Chengyun Liu. 3D parallel fully convolutional networks for real-time video wildfire smoke detection. *IEEE Transactions on Circuits and Systems for Video Technology*, 30(1):89–103, 2020.
- [11] Feiniu Yuan, Lin Zhang, Xue Xia, Boyang Wan, Qinghua Huang, and Xuelong Li. Deep smoke segmentation. *Neurocomputing*, 357:248–260, 2019.
- [12] Jianmei Zhang, Hongqing Zhu, Pengyu Wang, and Xiaofeng Ling. ATT squeeze U-Net: A lightweight network for forest fire detection and recognition. *IEEE Access*, 9:10858–10870, 2021.
- [13] Siyuan Yan, Jing Zhang, and Nick Barnes. Transmission-guided Bayesian generative model for smoke segmentation. In *Proceedings of the AAAI Conference on Artificial Intelligence*, volume 36, pages 3009–3017, 2022.
- [14] Ze Song, Xudong Kang, Xiaohui Wei, Jinyang Liu, Zheng Lin, and Shutao Li. Continuous feature representation for camouflaged object detection. *IEEE Transactions on Image Processing*, 34:5672–5685, 2025.

- [15] Weiwei Sun and Qian Du. Hyperspectral band selection: A review. *IEEE Geoscience and Remote Sensing Magazine*, 7(2):118–139, 2019.
- [16] Zijian Li, Mi Wang, and Shaoju Wang. Hyperspectral band selection via structural correlation and information measures. *IEEE Geoscience and Remote Sensing Letters*, 22, 2025.
- [17] Muhammad Ahmad, Sidrah Shabbir, Swalpa Kumar Roy, Danfeng Hong, Xin Wu, Jing Yao, Adil Mehmood Khan, Manuel Mazzara, Salvatore Distefano, and Jocelyn Chanussot. Hyperspectral image classification—traditional to deep models: A survey for future prospects. *IEEE Journal of Selected Topics in Applied Earth Observations and Remote Sensing*, 15:968–999, 2021.
- [18] Danfeng Hong, Lianru Gao, Jing Yao, Bing Zhang, Antonio Plaza, and Jocelyn Chanussot. Graph convolutional networks for hyperspectral image classification. *IEEE Transactions on Geoscience and Remote Sensing*, 59(7):5966–5978, 2020.
- [19] Bo Du, Yuxiang Zhang, Liangpei Zhang, and Dacheng Tao. Beyond the sparsity-based target detector: A hybrid sparsity and statistics-based detector for hyperspectral images. *IEEE Transactions on Image Processing*, 25(11):5345–5357, 2016.
- [20] Hao Sun, Xiangtao Zheng, Xiaoqiang Lu, and Siyuan Wu. Spectral–spatial attention network for hyperspectral image classification. *IEEE Transactions on Geoscience and Remote Sensing*, 58(5):3232–3245, 2020.
- [21] Shivam Pande and Biplab Banerjee. HyperLoopNet: Hyperspectral image classification using multiscale self-looping convolutional networks. *ISPRS Journal of Photogrammetry and Remote Sensing*, 183:422–438, 2022.
- [22] Shou Feng, Shengnan Wang, Congan Xu, Chunhui Zhao, Wei Li, and Ran Tao. Fractional domain information-enhanced hyperspherical prototype learning method for hyperspectral image open-set classification. *IEEE Transactions on Geoscience and Remote Sensing*, 63:5515117, 2025.

- [23] Bolin Fu, Xifeng Deng, Hongyuan Kuang, Zhaoyin Wang, and Donglin Fan. GFHMP: Gradual fusion framework of hyperspectral, multispectral, and panchromatic images using a novel spatial-spectral cross-fusion network. *IEEE Transactions on Geoscience and Remote Sensing*, 63:1–17, 2025.
- [24] Jinyang Liu, Shutao Li, Renwei Dian, Ze Song, and Lishan Tan. Asymptotic spectral mapping for hyperspectral image fusion. *IEEE Transactions on Circuits and Systems for Video Technology*, 35(4):3475–3485, 2025.
- [25] Hang Yao, Ya Zhang, Bolin Fu, Zhili Chen, Xing Zhang, and Tengfang Deng. Combination of UAV hyperspectral and LiDAR data for classifying karst wetland vegetation species using the ael-stacking and lime. *Journal of Remote Sensing*, 5:0452, 2025.
- [26] Jinyang Liu, Shutao Li, Heng Yang, Renwei Dian, and Yuanye Liu. Heterospectral structure compensation sampling for hyperspectral fusion computational imaging. *IEEE Transactions on Image Processing*, 34:7930–7942, 2025.
- [27] Thomas Cover and Peter Hart. Nearest neighbor pattern classification. *IEEE Transactions on Information Theory*, 13(1):21–27, 1967.
- [28] Barbara J. Knowlton and Larry R. Squire. The learning of categories: Parallel brain systems for item memory and category knowledge. *Science*, 262(5140):1747–1749, 1993.
- [29] Teuvo Kohonen. The self-organizing map. *Proceedings of the IEEE*, 78(9):1464–1480, 1990.
- [30] Jacob Goldberger, Geoffrey E. Hinton, Sam Roweis, and Russ R. Salakhutdinov. Neighbourhood components analysis. In *Advances in Neural Information Processing Systems*, volume 17, pages 1–8, 2004.
- [31] Pascal Mettes, Elise Van der Pol, and Cees Snoek. Hyperspherical prototype networks. In *Advances in Neural Information Processing Systems*, volume 32, pages 1–11, 2019.
- [32] Zhirong Wu, Yuanjun Xiong, Stella X. Yu, and Dahua Lin. Unsupervised feature learning via non-parametric instance discrimination. In

*Proceedings of the IEEE Conference on Computer Vision and Pattern Recognition*, pages 3733–3742, 2018.

- [33] Mathilde Caron, Ishan Misra, Julien Mairal, Priya Goyal, Piotr Bojanowski, and Armand Joulin. Unsupervised learning of visual features by contrasting cluster assignments. In *Advances in Neural Information Processing Systems*, volume 33, pages 9912–9924, 2020.
- [34] David Eigen, Marc’Aurelio Ranzato, and Ilya Sutskever. Learning factored representations in a deep mixture of experts. *arXiv preprint arXiv:1312.4314*, 2013.
- [35] Dmitry Lepikhin, HyoukJoong Lee, Yuanzhong Xu, Dehao Chen, Orhan Firat, Yanping Huang, Maxim Krikun, Noam Shazeer, and Zhifeng Chen. GShard: Scaling giant models with conditional computation and automatic sharding. *arXiv preprint arXiv:2006.16668*, 2020.
- [36] William Fedus, Barret Zoph, and Noam Shazeer. Switch Transformers: Scaling to trillion parameter models with simple and efficient sparsity. *Journal of Machine Learning Research*, 23(120):1–39, 2022.
- [37] Bryce Hopkins, Leo O’Neill, Fatemeh Afghah, Abolfazl Razi, Eric Rowell, Adam Watts, Peter Fule, and Janice Coen. Flame 2: Fire detection and modeling: Aerial multi-spectral image dataset. *IEEE DataPort*, 2023.
- [38] Enze Xie, Wenhui Wang, Zhiding Yu, Anima Anandkumar, Jose M. Alvarez, and Ping Luo. SegFormer: Simple and efficient design for semantic segmentation with Transformers. In *Advances in Neural Information Processing Systems*, volume 34, pages 12077–12090, 2021.
- [39] Marco Cuturi. Sinkhorn distances: Lightspeed computation of optimal transport. In *Advances in Neural Information Processing Systems*, volume 26, pages 1–9, 2013.
- [40] Tianfei Zhou and Wenguan Wang. Prototype-based semantic segmentation. *IEEE Transactions on Pattern Analysis and Machine Intelligence*, 46(10):6858–6872, 2024.

- [41] Lujian Yao, Haitao Zhao, Jingchao Peng, Zhongze Wang, and Kaijie Zhao. FoSp: Focus and separation network for early smoke segmentation. In *Proceedings of the AAAI Conference on Artificial Intelligence*, volume 38, pages 6621–6629, 2024.
- [42] Hengshuang Zhao, Jianping Shi, Xiaojuan Qi, Xiaogang Wang, and Jiaya Jia. Pyramid scene parsing network. In *Proceedings of the IEEE Conference on Computer Vision and Pattern Recognition*, pages 2881–2890, 2017.
- [43] Liang-Chieh Chen, Yukun Zhu, George Papandreou, Florian Schroff, and Hartwig Adam. Encoder-decoder with atrous separable convolution for semantic image segmentation. In *European Conference on Computer Vision*, pages 801–818, 2018.
- [44] Yuhui Yuan, Xilin Chen, and Jingdong Wang. Object-contextual representations for semantic segmentation. In *European Conference on Computer Vision*, pages 173–190. Springer, 2020.
- [45] Meng-Hao Guo, Cheng-Ze Lu, Qibin Hou, Zhengning Liu, Ming-Ming Cheng, and Shi-Min Hu. SegNeXt: Rethinking convolutional attention design for semantic segmentation. In *Advances in Neural Information Processing Systems*, volume 35, pages 1140–1156, 2022.
- [46] Bowen Cheng, Ishan Misra, Alexander G. Schwing, Alexander Kirillov, and Rohit Girdhar. Masked-attention mask transformer for universal image segmentation. In *Proceedings of the IEEE/CVF Conference on Computer Vision and Pattern Recognition*, pages 1290–1299, 2022.